nature physics

Article

https://doi.org/10.1038/s41567-023-02075-7

Programmable large-scale simulation of bosonic transport in optical synthetic frequency lattices

Received: 10 November 2022

Accepted: 28 April 2023

Published online: 29 May 2023

Check for updates

Alen Senanian **®** ^{1,2} ⋈, Logan G. Wright **®** ^{2,3}, Peter F. Wade⁴, Hannah K. Doyle² & Peter L. McMahon^{2,5} ⋈

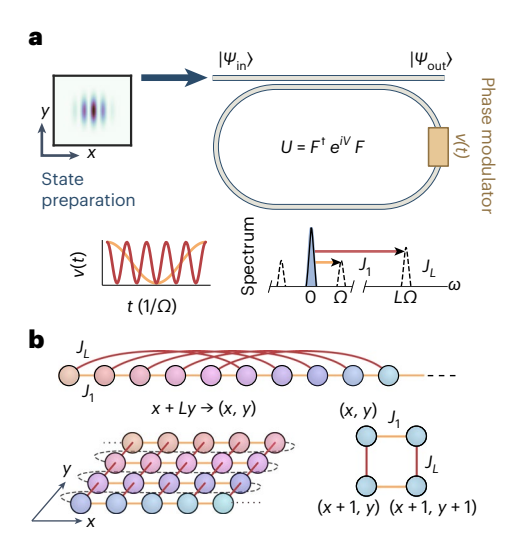
Photonic simulators using synthetic frequency dimensions have enabled flexible experimental analogues of condensed-matter systems. However, so far, such photonic simulators have been limited in scale, yielding results that suffer from finite-size effects. Here we present an analogue simulator capable of simulating large two-dimensional (2D) and 3D lattices, as well as lattices with non-planar connectivity. Our simulator takes advantage of the broad bandwidth achievable in photonics, allowing our experiment to realize programmable lattices with over 100,000 lattice sites. We showcase the scale of our simulator by demonstrating the extension of bandstructure spectroscopy from 1D to 2D and 3D lattices. We then report the direct observation of time-reversal symmetry-breaking in a triangular lattice in both momentum and real space, as well as site-resolved occupation measurements in a tree-like geometry that serves as a toy model in quantum gravity. Moreover, we demonstrate a method to excite arbitrary multisite states, which we use to study the response of a 2D lattice to both conventional and exotic input states. Our work highlights the scalability and flexibility of optical synthetic frequency dimensions. Future experiments building on our approach will be able to explore non-equilibrium phenomena in high-dimensional lattices and to simulate models with nonlocal higher-order interactions.

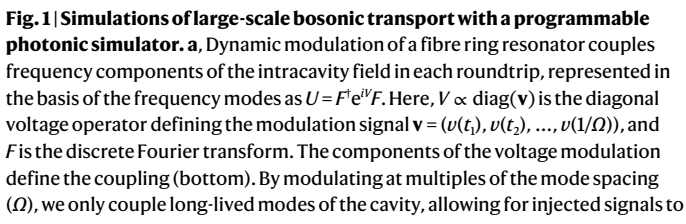
Simulations have long been used to understand emergent phenomena in complex many-body systems. Special-purpose analogue simulators trade off the generality of digital implementations for either scalability or access to regimes that are challenging for digital computers. In this regard, photonic analogue simulators¹⁻⁶ complement developments in platforms like superconducting circuits^{7,8} and ultracold atoms⁹ by enabling, in principle, extremely large-scale simulations. Photonic simulation has a long history and has led to the discovery of a variety of phenomena that are challenging to realize in conventional condensed-matter systems, such as topological phase

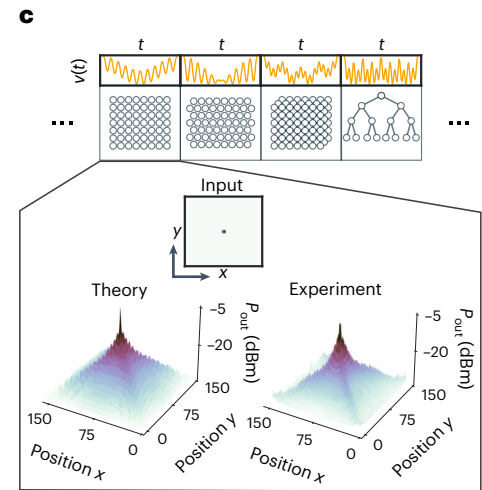
transitions^{10–14} and non-Hermitian exceptional points^{15–17}, which in turn has led to new photonic devices with applications far beyond basic physical science^{18,19}.

Although telecommunication technologies routinely utilize the high bandwidth inherent to optics, harnessing the frequency parallelism of light for large-scale analogue simulation has largely remained unexplored. One promising approach is to implement synthetic frequency dimensions^{6,20-24}, in which optical frequency modes are mapped to lattice sites to perform bosonic analogue simulations. Simulators using synthetic frequency dimensions have been shown to

¹Department of Physics, Cornell University, Ithaca, NY, USA. ²School of Applied and Engineering Physics, Cornell University, Ithaca, NY, USA. ³NTT Physics and Informatics Laboratories, NTT Research, Inc., Sunnyvale, CA, USA. ⁴School of Electrical and Computer Engineering, Cornell University, Ithaca, NY, USA. ⁵Kavli Institute at Cornell for Nanoscale Science, Cornell University, Ithaca, NY, USA. ⊠e-mail: as3656@cornell.edu; pmcmahon@cornell.edu







propagate in frequency for many multiples of the roundtrip time. **b**, Engineered long-range coupling maps the 1D spectrum to an $L \times L$ 2D lattice with twisted boundary conditions. As L grows large, the lattice approaches a smooth 2D plane. **c**, A set of voltage signals defining lattices in 2D and 3D (top; see the main text and Supplementary Fig. 7 for details), and the response to a single frequency drive (single-site) for a twisted 2D square lattice with over 20,000 lattice sites compared with tight-binding simulations of a 2D square lattice (bottom).

be versatile, implementing synthetic electric and magnetic fields²⁵⁻²⁷, non-Hermitian coupling^{6,28} and nonlinear interactions^{27,29}. So far, however, these demonstrations have been confined to small lattice sizes, with limited programmability and restricted initial conditions.

In this Article we demonstrate a frequency-mode-based platform that can simulate transport of arbitrary excitations in planar and non-planar optical lattices with up to 100,000 sites-orders of magnitude greater than achieved previously in photonic simulators with programmable geometry³⁰. By pursuing a dense spectrum with megahertz mode spacing, we leverage developments in both optical frequency combs and high-frequency optoelectronics to manipulate and probe a large number of optical frequency modes in a ring cavity. Additionally, these technologies enable a wide-bandwidth measurement scheme and arbitrary encoding of both the amplitude and phase of input states, allowing fine resolution and control of bosonic transport. We leverage the scale and programmability of our simulator with three key demonstrations. First, our simulator can read out momentum-space features with high resolution, enabling us to measure bandstructures of various multidimensional lattices. Second, we observe both the real- and momentum-space signatures of time-reversal symmetry-breaking due to an effective gauge field in a two-dimensional (2D) triangular lattice, an important step towards the realization of the photonic quantum-valley Hall effect³¹⁻³³. Third, we observe hierarchical transport across several orders of magnitude of length scales within a non-planar tree-like network, a toy model for quantum gravity and p-adic anti-de Sitter/conformal field theory (AdS/ CFT) correspondence^{34,35}.

The class of Hamiltonians that our system is able to simulate is given by

$$H = \sum_{i < j} J_{i-j} a_i^{\dagger} a_j + \text{H.c.}$$
 (1)

Hamiltonians in this class describe non-interacting bosons on translationally invariant lattices. a_l^{\dagger} and a_l are, respectively, the bosonic creation and annihilation operators for the lth lattice site. The lattice

geometries are defined by the complex tunnelling rates $J_k = |J_k| \mathrm{e}^{\mathrm{i}\phi_k}$, which encode the translationally invariant coupling of sites a distance k apart with amplitude $|J_k|$ and phase ϕ_k . The main goal of the photonic simulator we present in this work is to be able study the transport of a variety of single-particle excitations in any Hamiltonian in the class defined by equation (1), where the complex parameters J_k can be programmed arbitrarily—this allows us to study a diversity of different lattices, including those that are multidimensional.

In the synthetic-frequency-dimensions approach that we adopt, the lattice operators a_l , a_l^{\dagger} are associated with the *l*th frequency mode of an optical cavity, spaced apart by Ω (the free spectral range (FSR) of the cavity). The tunnelling rates $(J_k)_{k=1,2,3,...}$ are physically realized using a phase modulator within the optical cavity (Fig. 1a) – intuitively, the modulator creates optical sidebands at the frequencies contained in the modulation signal v(t) and, by setting these sidebands at harmonics of Ω , these sidebands cause coupling between cavity modes. Additionally, by setting the amplitudes and phases of frequency components in v(t) appropriately, different lists of tunnelling amplitudes $(|J_k|)$ and relative phases (ϕ_{ι}) can be programmed (Fig. 1a), which in turn realize different lattice geometries (Fig. 1c). Our simulator includes a gain/ loss balance term in the Hamiltonian, but this is kept close to zero. Additionally, phase modulation at Ω produces higher-order sidebands, but these can be suppressed to negligible amplitudes by appropriately choosing the modulation voltage (Methods).

Although the Hamiltonian in equation (1) nominally describes a 1D lattice, we can implement effective higher-dimensional lattices by suitably programming the couplings (J_k) to reflect the local geometry of a target higher-dimensional lattice. For example, an effective $L \times L$ 2D square lattice can be realized in a nonlocal 1D lattice by coupling nearest-neighbours and Lth nearest-neighbours, that is, $(J_k)_{k=1,2,3,...} = (J_1, 0, ..., 0, J_L, 0, ...)$ (Fig. 1b). This produces a 2D lattice with a twisted boundary condition^{20,36}, and only approximates a true 2D lattice once L is made to be very large. Here, any local excitation with finite lifetime will become insensitive to the boundary. Thus, by pursuing a large number of modes, we can realize effective lattices in higher dimensions that approximate the true physics. The vanishing effects of the

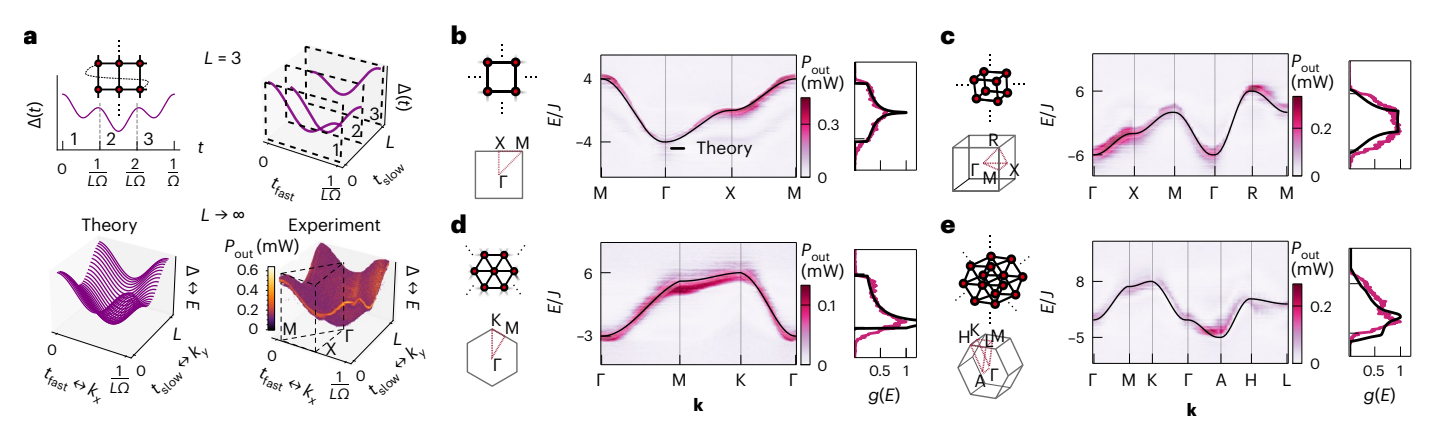


Fig. 2 | Optical bandstructure measurements of 2D and 3D lattices. a, Top: the bandstructure for a twisted 2D square lattice is measured from the time-domain response of the cavity to scanning single-frequency injection as a function of the detuning Δ (ref. 22), here demonstrated using a pedagogical example with linear lattice size L=3. This time-trace output is sliced into chunks of length L, allowing the reconstruction of a full 2D bandstructure measured in a single shot (Supplementary Fig. 9). Bottom: reconstructed bandstructure for a 2D square lattice with large L, comparing theoretical (left) with experimental (right) results for L=100. As L grows large, the effect of the twisted boundary condition

in the bandstructure becomes negligible, and the measured bandstructure approximates that of a regular 2D square lattice. **b**, Data of the full bandstructure plotted along slices that connect special points of the Brillouin zone, compared with theoretical results for a true 2D square lattice (black line). These points (highlighted bottom left) denote locations in momentum space with high symmetry. The density of states g(E) is directly measured by summing the time-domain response (right). **c**-**e**, Bandstructures and density of states for a 2D triangular lattice (L = 100) (**d**), 3D square lattice (L = 28) (**e**) and 3D hexagonal lattice (L = 28) (**f**).

twisted boundary condition can be seen in the steady-state response to a single-site excitation in the comparison shown in Fig. 1c between our experiment and simulations of a true 2D tight-binding lattice with hard boundary conditions.

The frequency-multiplexed platform has a convenient encoding of reciprocal space for lattice systems. In the mapping from lattice sites to frequency modes, time maps to momentum²². Therefore, because the Fourier components of the modulation signal define the connectivity, the modulation signal in the time domain defines the bandstructure. For a 1D lattice, this correspondence is exact: the modulation signal $v(t) = -V_0 \cos(\Omega t)$ couples nearest-neighbour modes, implementing a 1D tight-binding chain with bandstructure $E(k) = -J\cos(ka)$. Here the lattice spacing a is identified with the mode spacing Ω , and momentum k with time t. More generally, the action of phase modulation on the frequency modes can be expressed as a unitary operator $U = F^{\dagger} e^{iV} F$. where F is the discrete Fourier transform, and $V \propto \text{diag}(\mathbf{v})$ is a diagonal matrix whose values are proportional to the voltage signal $\mathbf{v} = (v(t_1), v(t_2), ..., v(1/\Omega))$. In our simulator, the operator *U* implements the time evolution defined by the Hamiltonian in equation (1). Thus, the modulation signal v(t) defines the time evolution in a diagonal basis, and therefore encodes energy eigenvalues of the lattice, that is, the bandstructure. As a consequence, this permits us to encode arbitrary lattices that have a single-band bandstructure. Additionally, it provides us direct access to momentum-space lattice measurements²²

To extend the momentum-to-time analogy to 2D and 3D, we require a large enough number of modes to eliminate the finite-size effects from the twisted boundary condition. For the above example of an effective 2D lattice, slices of the bandstructure along the slow axis (that is, the axis corresponding to transport along nearest neighbours) suffer from an asymmetry near the boundaries of the Brillouin zone (Fig. 2a), prominent for small L. This is due to the twisted boundary conditions, which makes the two directions no longer independent, because L hops along Ω will reach the same position as a single hop along $L\Omega$. Concretely, the asymmetry can be seen by comparing the two-tone signal we use to generate a 2D lattice, $v(t) = -2V_0\cos(\Omega t) - 2V_0\cos(L\Omega t)$, and a true 2D tight-binding lattice with nearest-neighbour hopping, which has a bandstructure $E(\mathbf{k}) = -2J\cos(k_x a) - 2J\cos(k_y a)$. The latter has two independent reciprocal lattice vectors, k_x and k_y . For $L \gg 1$, however, we can rely on a separation of timescales and treat

 $\Omega' = L\Omega$ as an effective independent degree of freedom. This approach can be extended to higher-dimensional lattices; for example, for a 3D square lattice, Ω , $L\Omega$ and $L^2\Omega$ are the independent degrees of freedom.

Figure 2a outlines how we extend the methods introduced in ref. 22 to measure the bandstructure of a 2D lattice in a single shot, then slice up the measured bandstructure in periods of $T_{\rm fast}$ = 1/ $L\Omega$ to reconstruct the 2D full bandstructure. See the Methods and Supplementary Figs. 9 and 10 for full details on this reconstruction. As $L \to \infty$, the bandstructure of our effective 2D square lattice approaches that of a regular 2D square lattice, as seen when comparing Fig. 2a and 2b. Slices through high symmetry points of the full bandstructure are shown in Fig. 2b–e for 2D square, 2D triangular, 3D simple cubic and 3D hexagonal lattices, along with the respective density of states for each. Theoretical curves for ordinary tight-binding lattices are shown in black.

High-bandwidth telecommunications optoelectronics enable the study of transport in our platform for arbitrary input states. Our scheme is enabled by 12-GHz electro-optic modulation, as summarized schematically in Fig. 3a. This technique allows us to specify the amplitude and phases of input excitations for up to ~4,000 lattice sites, limited primarily by a bandpass filter (Methods). Figure 3b presents experimental measurements of various input states, including standing wavepacket eigenstates, angular wavepackets and a Cornell 'C'. The right columns display their respective steady-state response. Here, we are continuously exciting local states and observing their steady-state dynamics in the presence of loss. The full control over both amplitude and phase enables us to excite states with net momentum. Figure 3c shows the steady-state response of momentum eigenstates of a 2D square lattice enveloped with a Gaussian for a discrete set of nonzero input momenta. We can directly observe locally excited momentum states propagating in different directions. The momentum of each input state is labelled by its respective momentum distribution within the Brillouin zone, shown in the left column of Fig. 3c.

By programming the phases and detunings of the coupling Hamiltonian (equation (1)), we implemented synthetic magnetic and electric fields, respectively (Supplementary Fig. 18 provides measurements for synthetic electric fields) $^{25,26,37-45}$, as well as non-Hermitian models (Supplementary Figs. 19 and 20 provide realizations of the Hatano–Nelson model in 1D and 2D). Figure 4 shows the effect of a synthetic gauge field applied to a 2D triangular lattice, giving rise to a global zero magnetic

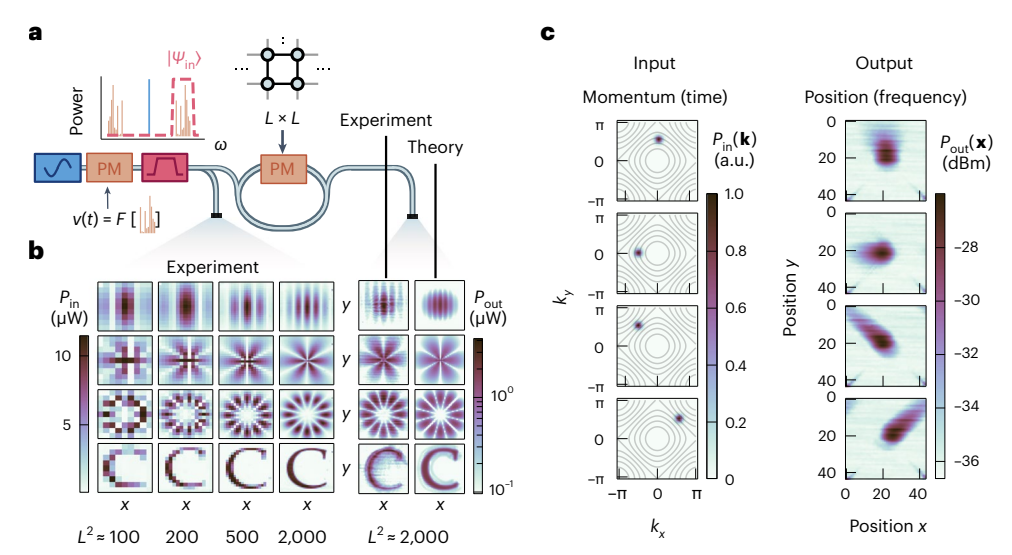
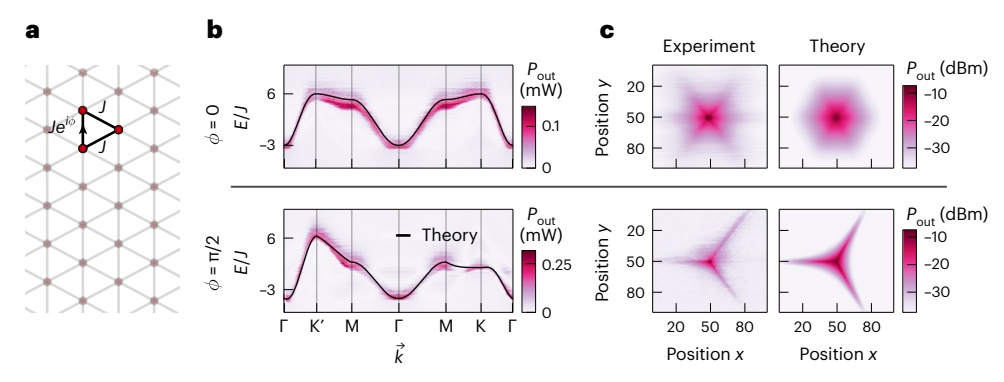


Fig. 3 | **Input state preparation. a**, Scheme for preparing arbitrary input states. Using a phase modulator (PM), a single frequency tone is modulated with a RF signal encoding both amplitude and phase of a given state, producing symmetric sidebands (orange spectrum). The initial tone and the unwanted sideband is then rejected with a bandpass filter (red envelope), leaving only the positive sidebands, which are sent into the cavity. **b**, Experimental measurements of input states for an increasing number of modes programmed in the input signal for (top to bottom) a standing wavepacket, an angular wave enveloped with a Gaussian centred at zero, a higher angular state enveloped with an offset radial

Gaussian, and the Cornell University logo. The steady-state outputs of these states for a 2D $L \times L$ square lattice are shown to the right, along with a comparision with theory. **c**, We excited the momentum eigenstates of a 2D square lattice with momenta in various directions, enveloped with a Gaussian. Left: representation of the input state in momentum space, $\mathbf{k} = (k_x, k_y)$. Right: the experimental steady state in position space $\mathbf{x} = (x, y)$. Here, local momentum eigenstates are continuously excited at the centre, and propagate with a well-defined momentum before decaying.



 $\label{lem:fig.4} \textbf{Fig. 4} | \textbf{Time-reversal symmetry-breaking in a 2D triangular lattice due} \\ \textbf{to an effective gauge field. a}, \textbf{Complex hopping terms induce a nonzero} \\ \textbf{local magnetic flux within a plaquette of a triangular lattice. Here, a relative phase is added to one of three directions incident on a given lattice site. \textbf{b}}, \textbf{The} \\ \textbf{introduction of the magnetic field breaks time-reversal symmetry, as can be seen} \\ \textbf{in the asymmetry of the } \textit{K} \text{ and } \textit{K}' \text{ points in the bandstructure after performing} \\ \textbf{and } \textit{K}' \text{ points in the bandstructure after performing} \\ \textbf{and } \textit{K}' \text{ points in the bandstructure after performing} \\ \textbf{and } \textit{K}' \text{ points in the bandstructure after performing} \\ \textbf{and } \textit{K}' \text{ points in the bandstructure after performing} \\ \textbf{and } \textit{K}' \text{ points in the bandstructure after performing} \\ \textbf{and } \textit{K}' \text{ points in the bandstructure after performing} \\ \textbf{and } \textit{K}' \text{ points in the bandstructure after performing} \\ \textbf{and } \textit{K}' \text{ points in the bandstructure after performing} \\ \textbf{and } \textit{K}' \text{ points in the bandstructure after performing} \\ \textbf{and } \textit{K}' \text{ points in the bandstructure after performing} \\ \textbf{and } \textit{K}' \text{ points in the bandstructure after performing} \\ \textbf{and } \textit{K}' \text{ points in the bandstructure after performing} \\ \textbf{and } \textit{K}' \text{ points in the bandstructure after performing} \\ \textbf{and } \textit{K}' \text{ points in the bandstructure after performing} \\ \textbf{and } \textit{K}' \text{ points in the bandstructure after performing} \\ \textbf{and } \textit{K}' \text{ points in the bandstructure after performing} \\ \textbf{and } \textit{K}' \text{ points in the bandstructure after performing} \\ \textbf{and } \textit{K}' \text{ points in the bandstructure after performing} \\ \textbf{and } \textit{K}' \text{ points in the bandstructure after performing} \\ \textbf{and } \textit{K}' \text{ points in the bandstructure after performing} \\ \textbf{and } \textit{K}' \text{ points in the bandstructure after performing} \\ \textbf{and } \textit{K}' \text{ points in the bandstructure after performing} \\ \textbf{and } \textit{K}' \text{ points in the bandstructure after performing} \\ \textbf{and } \textit{K}$

Peierls substitution (bottom). \mathbf{c} , Measured steady-state spectral response due to a single-site injection under the influence of the synthetic local magnetic field. The presence of the synthetic field leads to a departure from six-fold symmetry to three-fold symmetry in the transport. Experimental data (left) are compared with simulations (right).

field, but nonzero local magnetic field. Adding a relative phase along nearest-neighbour hoppings results in an accumulated phase of either $e^{i\phi}$ or $e^{-i\phi}$, indicating a local nonzero magnetic flux going around each plaquette. The sign of the accumulated phase alternates between neighbouring plaquettes, making the total magnetic flux through the lattice vanish globally. Shown in Fig. 4b, the addition of this field breaks time-reversal symmetry, which, for the triangular and honeycomb lattices, maps the K points to K' points 31 . This results in a reduction from a six-fold symmetry to a three-fold symmetry in the transport of injected light, where propagation of light is prohibited in certain directions, as shown in the heterodyne measurements of the steady-state density (Fig. 4). This time-reversal symmetry-breaking with local nonzero fields is one key ingredient in observations of the quantum-valley Hall effect seen in honeycomb lattices $^{31-33}$.

In addition to lattices found in traditional condensed-matter systems, our photonic simulator is capable of simulating systems not realizable in crystalline materials. Systems with non-planar connectivity are particularly interesting given that their realization in solid-state systems is impractical, yet they contain rich physics. Periwal and colleagues⁹ recently experimentally demonstrated a simulation of a graph with exotic long-range connectivity given by

$$J_{i-j} \propto \begin{cases} |i-j|^s & |i-j| = 2^n, n \in \{0, 1, 2, ...\} \\ 0 & \text{otherwise} \end{cases}$$
 (2)

This describes a system that can be continuously changed, using the parameter s, from an Archimedean-geometry regime in which

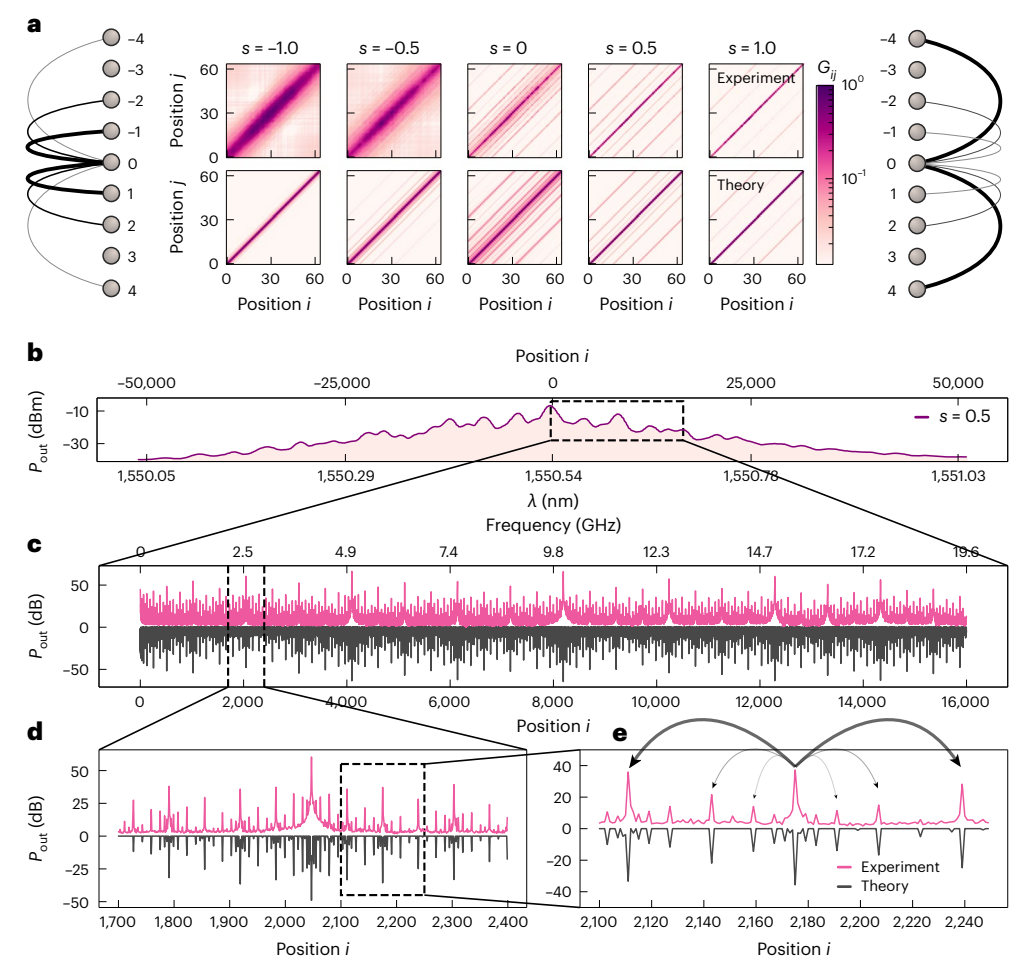


Fig. 5 | Simulations of bosonic transport in a tree-like geometry with a graph comprising over 100,000 sites. a, Non-equilibrium correlation measurements for a 1D chain with nonlocal connectivity, characterized by the degree of locality s (equation (2)). As s is tuned from -1 (left) to +1 (right), the correlations transition from locally decaying to tree-like $^{\circ}$. The top row presents experimental data, and bottom row shows the theory. The lattice cartoons on the left and right schematically show the coupling form for a single lattice site (position 0).

 $\label{eq:bound} \textbf{b}, Optical-spectrum measurement for the response to a single-site injection with $s=0.5$, showing a measurable steady-state population in >100,000 lattice sites. <math display="block"> \textbf{c}-\textbf{e}, RF \text{ spectrum measurements showing the lattice occupation with single-site resolution of the zoom-in in the full optical spectrum, comparing with simulations for windows of 20 GHz (\textbf{c}), 500 MHz (\textbf{d}) and 100 MHz (\textbf{e}). Theoretical results have been inverted for clarity.$

correlations between sites decay with distance |i-j|, to a non-Archimedean-geometry regime in which the correlations between sites have a tree-like structure. The hierarchical geometry of this tree-like system is a toy model for p-adic AdS/CFT correspondence³⁵, studied previously using atomic ensembles in an optical lattice with 16 sites°, but shown here in a photonic system. We experimentally show this transition in Fig. 5a in the measurements of correlations of the lattice as s is tuned (the Methods provides details on the correlation measurements and Supplementary Fig. 17 presents another example). Near the transition, at s = 0.5, the lattice exhibits both strong local and nonlocal connectivity, resulting in dense yet extremely large lattices, as shown in both optical-spectrum measurements in Fig. 5b and radiofrequency (RF) spectrum measurements in Fig. 5c.

Although some graphs, such as the tree-like example depicted in Fig. 5, result in occupations that span 100,000 or more lattice sites, quantifying the absolute size of our simulator requires some nuance. On the one hand, based on the dispersion and bandwidth of the elements inside the cavity, we believe the lattices we simulate span several terahertz, corresponding to millions of lattice sites. On the other hand, as in real material systems, local excitations in lattices that have only short- or medium-range connectivity will typically not be able to propagate to very distant sites before their amplitude decays below

the noise floor of the detector. For example, in the experiments we performed with 2D lattices, the steady-state response was detectable in at most -10⁴ lattice sites in the vicinity of the injected wavepacket (Fig. 1c and Supplementary Fig. 16).

The demonstrations described in this Article cover only a small fraction of the bosonic physics that can be simulated with frequencydomain coupling of photonic modes. Simple modifications to the presented experimental set-up, such as dispersion compensation, reducing total intracavity loss, and reducing the input power far below the gain-saturation power, should substantially increase the number of accessible lattice sites. Additionally, stabilizing the cavity phase with respect to the phase of the input state would remove decoherence effects limiting the propagation of our input excitations. With these upgrades, observing dynamics on lattices spanning millions of sites (or more) would become feasible. By adding multiple spatial modes⁴⁶ or bidirectional propagation¹², simulations of topological phenomena found in higher-dimensional gapped multiband systems may be realized. With coupled cavities, defects and hard lattice edges²⁴ may be implemented. In our simulator, this would enable the study of propagating edge modes in high-dimensional lattices. By varying the intracavity phase modulation over multiple cavity periods, time-dependent lattices may be realized, which would allow

the study of new non-equilibrium phases⁴⁷ and the implementation of very wide convolutional optical neural networks⁴⁸. Similarly, the use of stroboscopic modulation, as opposed to continuouswave modulation, would enable timed measurements of transient dynamics, such as observing band evolutions⁴⁹ and time-resolved spectral measurements. In unmodulated cavities, Kerr nonlinearities give rise to locked combs defined by dissipative cavity solitons⁵⁰. In the frequency domain, the Kerr effect produces highly nonlocal, four-mode interactions ^{27,29}. Because Kerr interactions may be programmed by modifying intracavity dispersion and spectral loss, and by introducing additional mode families⁴⁶, it should be possible to realize both new types of intricately tailored Kerr frequency comb, as well as simulations of the statistical mechanics of graphs with higher-order interactions⁴⁷, which should allow the observation of emergent multistable states and abrupt synchronization (mode-locking) transitions.

Photonic simulators have, over the past decade, been established as robust platforms for exploring condensed-matter phenomena, including some that have been inaccessible in material systems. In this Article we have demonstrated a large-scale, programmable photonic simulator using synthetic frequency dimensions. We have used our simulator to study several models with a variety of different geometries, including a lattice with tree-like connectivity that has, to our knowledge, not previously been realized outside of cold-atom experiments and that would be impractical to realize at scale in most simulator platforms without the use of synthetic dimensions due to the model's highly nonlocal interactions. Looking to the future, our simulator could be extended to even larger sizes through dispersion and loss engineering, modified to support the study of topological phenomena, and augmented with a nonlinearity that induces higher-order interactions between lattice sites. With extensions to fully utilize the many terahertz of bandwidth that is, in principle, available in optics, programmable synthetic-frequency-dimension photonic simulators may soon explore high-dimensional nonlinear physics, both near and far from equilibrium. At all scales, advances in this platform will benefit the development of tailored light sources and optical signal processors. However, it is in the terahertz-spanning ultra-large-scale regime that photonic simulators seem most compelling to us as analogue simulators, with prospects to explore—and discover—entirely new and unexpected physical phenomena.

Online content

Any methods, additional references, Nature Portfolio reporting summaries, source data, extended data, supplementary information, acknowledgements, peer review information; details of author contributions and competing interests; and statements of data and code availability are available at https://doi.org/10.1038/s41567-023-02075-7.

References

- Lahini, Y. et al. Observation of a localization transition in quasiperiodic photonic lattices. *Phys. Rev. Lett.* **103**, 013901 (2009).
- Lin, Q., Xiao, M., Yuan, L. & Fan, S. Photonic Weyl point in a two-dimensional resonator lattice with a synthetic frequency dimension. *Nat. Commun.* 7, 13731 (2016).
- Harris, N. C. et al. Quantum transport simulations in a programmable nanophotonic processor. *Nat. Photon.* 11, 447–452 (2017).
- Muniz, A. L. M., Wimmer, M., Bisianov, A., Morandotti, R. & Peschel, U. Collapse on the line—how synthetic dimensions influence nonlinear effects. Sci. Rep. 9, 9518 (2019).
- 5. Wang, P. et al. Localization and delocalization of light in photonic moiré lattices. *Nature* **577**, 42–46 (2020).
- Wang, K. et al. Generating arbitrary topological windings of a non-Hermitian band. Science 371, 1240–1245 (2021).

- Hung, J. S. C. et al. Quantum simulation of the bosonic Creutz ladder with a parametric cavity. *Phys. Rev. Lett.* 127, 100503 (2021).
- 8. Karamlou, A. H. et al. Quantum transport and localization in 1D and 2D tight-binding lattices. *npj Quantum Inf.* **8**, 35 (2022).
- Periwal, A. et al. Programmable interactions and emergent geometry in an array of atom clouds. *Nature* 600, 630–635 (2021).
- Ozawa, T. et al. Topological photonics. Rev. Mod. Phys. 91, 015006 (2019).
- Lustig, E. et al. Photonic topological insulator in synthetic dimensions. *Nature* 567, 356–360 (2019).
- Dutt, A. et al. A single photonic cavity with two independent physical synthetic dimensions. Science 367, 59–64 (2020).
- 13. Lustig, E. & Segev, M. Topological photonics in synthetic dimensions. *Adv. Opt. Photon.* **13**, 426–461 (2021).
- 14. Leefmans, C. et al. Topological dissipation in a time-multiplexed photonic resonator network. *Nat. Phys.* **18**, 442–449 (2022).
- Eichelkraut, T. et al. Mobility transition from ballistic to diffusive transport in non-Hermitian lattices. *Nat. Commun.* 4, 2533 (2013).
- Hodaei, H. et al. Enhanced sensitivity at higher-order exceptional points. Nature 548, 187–191 (2017).
- Weidemann, S., Kremer, M., Longhi, S. & Szameit, A. Coexistence of dynamical delocalization and spectral localization through stochastic dissipation. *Nat. Photon.* 15, 576–581 (2021).
- 18. Bandres, M. A. et al. Topological insulator laser: experiments. *Science* **359**, eaar4005 (2018).
- Hokmabadi, M. P., Schumer, A., Christodoulides, D. N. & Khajavikhan, M. Non-Hermitian ring laser gyroscopes with enhanced Sagnac sensitivity. *Nature* 576, 70–74 (2019).
- 20. Schwartz, A. & Fischer, B. Laser mode hyper-combs. *Opt. Express* **21**, 6196–6204 (2013).
- Ozawa, T., Price, H. M., Goldman, N., Zilberberg, O. & Carusotto, I. Synthetic dimensions in integrated photonics: from optical isolation to four-dimensional quantum Hall physics. *Phys. Rev. A* 93, 043827 (2016).
- 22. Dutt, A. et al. Experimental band structure spectroscopy along a synthetic dimension. *Nat. Commun.* **10**, 3122 (2019).
- Hu, Y., Reimer, C., Shams-Ansari, A., Zhang, M. & Lončar, M. Realization of high-dimensional frequency crystals in electro-optic microcombs. Optica 7, 1189–1194 (2020).
- 24. Dutt, A. et al. Creating boundaries along a synthetic frequency dimension. *Nat. Commun.* **13**, 3377 (2022).
- Bersch, C., Onishchukov, G. & Peschel, U. Experimental observation of spectral Bloch oscillations. Opt. Lett. 34, 2372–2374 (2009).
- 26. Lee, N. R. et al. Propagation of microwave photons along a synthetic dimension. *Phys. Rev. A* **101**, 053807 (2020).
- 27. Englebert, N. et al. Bloch oscillations of driven dissipative solitons in a synthetic dimension. *Nat. Phys.* 1–8 (2023)
- Wang, K., Dutt, A., Wojcik, C. C. & Fan, S. Topological complexenergy braiding of non-Hermitian bands. *Nature* 598, 59–64 (2021).
- Tusnin, A. K., Tikan, A. M. & Kippenberg, T. J. Nonlinear states and dynamics in a synthetic frequency dimension. *Phys. Rev. A* 102, 023518 (2020).
- Yuan, L., Dutt, A. & Fan, S. Synthetic frequency dimensions in dynamically modulated ring resonators. APL Photonics 6, 071102 (2021).
- Haldane, F. D. M. Model for a quantum Hall effect without Landau levels: condensed-matter realization of the 'Parity Anomaly'. Phys. Rev. Lett. 61, 2015–2018 (1988).
- 32. Mak, K. F., McGill, K. L., Park, J. & McEuen, P. L. The valley Hall effect in MoS₂ transistors. *Science* **344**, 1489–1492 (2014).

- Jiménez-Galán, Á., Silva, R. E. F., Smirnova, O. & Ivanov, M. Lightwave control of topological properties in 2D materials for sub-cycle and non-resonant valley manipulation. *Nat. Photon.* 14, 728–732 (2020).
- Gubser, S. S., Jepsen, C., Ji, Z. & Trundy, B. Continuum limits of sparse coupling patterns. *Phys. Rev. D* 98, 045009 (2018).
- 35. Bentsen, G. et al. Treelike interactions and fast scrambling with cold atoms. *Phys. Rev. Lett.* **123**, 130601 (2019).
- Yuan, L., Xiao, M., Lin, Q. & Fan, S. Synthetic space with arbitrary dimensions in a few rings undergoing dynamic modulation. *Phys. Rev. B* 97, 104105 (2018).
- D'Errico, A. et al. Bloch-Landau-Zener dynamics induced by a synthetic field in a photonic quantum walk. APL Photonics 6, 020802 (2021).
- 38. Li, G. et al. Dynamic band structure measurement in the synthetic space. *Sci. Adv.* **7**, eabe4335 (2021).
- Chen, H. et al. Real-time observation of frequency Bloch oscillations with fibre loop modulation. *Light Sci. Appl.* 10, 48 (2021).
- Yuan, L. & Fan, S. Bloch oscillation and unidirectional translation of frequency in a dynamically modulated ring resonator. *Optica* 3, 1014–1018 (2016).
- Qin, C. et al. Spectrum control through discrete frequency diffraction in the presence of photonic gauge potentials. *Phys. Rev. Lett.* 120, 133901 (2018).
- Qin, C., Yuan, L., Wang, B., Fan, S. & Lu, P. Effective electric-field force for a photon in a synthetic frequency lattice created in a waveguide modulator. *Phys. Rev. A* 97, 063838 (2018).
- 43. Miyake, H., Siviloglou, G. A., Kennedy, C. J., Burton, W. C. & Ketterle, W. Realizing the Harper Hamiltonian with laser-assisted tunneling in optical lattices. *Phys. Rev. Lett.* **111**, 185302 (2013).

- 44. Yuan, L. & Fan, S. Three-dimensional dynamic localization of light from a time-dependent effective gauge field for photons. *Phys. Rev. Lett.* **114**, 243901 (2015).
- Peterson, C. W., Benalcazar, W. A., Lin, M., Hughes, T. L. & Bahl, G. Strong nonreciprocity in modulated resonator chains through synthetic electric and magnetic fields. *Phys. Rev. Lett.* 123, 063901 (2019).
- 46. Wright, L. G., Christodoulides, D. N. & Wise, F. W. Spatiotemporal mode-locking in multimode fiber lasers. *Science* **358**, 94–97 (2017).
- 47. Battiston, F. et al. The physics of higher-order interactions in complex systems. *Nat. Phys.* **17**, 1093–1098 (2021).
- Fan, L. et al. Multidimensional convolution operation with synthetic frequency dimensions in photonics. *Phys. Rev. Appl.* 10, 34088 (2022).
- 49. Yu, D., Peng, B., Chen, X., Liu, X.-J. & Yuan, L. Topological holographic quench dynamics in a synthetic frequency dimension. *Light Sci. Appl.* **10**, 209 (2021).
- Kippenberg, T. J., Gaeta, A. L., Lipson, M. & Gorodetsky, M. L. Dissipative Kerr solitons in optical microresonators. *Science* 361, eaan8083 (2018).

Publisher's note Springer Nature remains neutral with regard to jurisdictional claims in published maps and institutional affiliations.

Springer Nature or its licensor (e.g. a society or other partner) holds exclusive rights to this article under a publishing agreement with the author(s) or other rightsholder(s); author self-archiving of the accepted manuscript version of this article is solely governed by the terms of such publishing agreement and applicable law.

© The Author(s), under exclusive licence to Springer Nature Limited 2023

Methods

Experimental details

The experimental set-up, shown schematically in Supplementary Fig. 1. consists of a long fibre ring with FSR of Ω = 1.226045 MHz, modulated with a 40-GHz phase modulator to produce the lattices described in the main text and the Supplementary Information. The losses in the cavity are compensated by a semiconductor optical amplifier (SOA). The initialization of arbitrary input states is enabled by filtering modulations of an injection. The modulation of both the input-state phase modulator and the cavity phase modulator are controlled by a single, multichannel arbitrary waveform generator (AWG). The injection laser serves both as a local oscillator for heterodyne detection, and for exciting input states. For high-bandwidth heterodyne detection, roughly half of the injection is sent through a phase modulator to prepare the input state before entering the cavity, while the other half is sent to recombine with the cavity output to produce 12-GHz beats. For full details, see Supplementary Figs. 1 and 13. The prescription of initializing input states results in 20 dB of insertion loss, but more than 30 dB of isolation between the filtered sideband and the local oscillator (LO), resulting in a clean single-sideband modulation. An initial amplifer is placed before the 50:50 splitter for compensating this insertion loss. After passing through the state-preparation module, the polarization of the prepared input state is set to align with the crystal axis of the intracavity electro-optic modulator (EOM). Coupling into and out of the cavity is done with 99:1 beamsplitters. Finally, the output of the cavity is combined with the LO before being detected by a photodetector, resulting in a 12-GHz heterodyne detection of the output. One component of resultant RF signal is amplified before being sent to an oscilloscope for single-shot bandstructure spectroscopy in the time domain. The other component of the RF signal is sent to the spectrum analyser (Tektronix RSA5126A) to perform direct readout of the lattice over 26 GHz. For bandstructure measurements, the heterodyne arm is turned off. The spectrum measured in Fig. 5b was measured with an optical spectrum analyser.

The intracavity SOA compensates for roundtrip losses in the cavity. However, the SOA contributes substantially to noise via the unwanted production of amplified spontaneous emission (ASE). To reduce ASE, a filter was placed in the cavity, and roundtrip losses were minimized to reduce the operating point of the SOA. The cavity losses were reduced to 5 dB, 4 dB of which originated from the insertion loss of the cavity EOM. In addition to limiting the noise, reducing the operating point of the SOA has the added benefit of reducing the contribution of ASE to the gain saturation. For a large ratio of input power to saturating power, transport of the optical power along the 1D chain is limited. From simulations, we find that a ratio of $P_{\text{seed}}/P_{\text{sat}} < 1/100$ is enough to reach thousands of modes above the noise floor of our set-up. The right side of Supplementary Fig. 3 shows the experimental measured value of gain saturation at ~4 dBm, so, for all of the measurements in the main text, we had an input power of below -20 dBm going into the cavity.

To instantiate a lattice with a large numbers of sites, knowledge of the cavity FSR is needed to within ~10 Hz to sustain the required coherence over many roundtrips. This was carefully measured using a number of methods (providing course-grained or fine-grained characterization). In a first step, we measured the FSR by exciting the cavity far above the lasing threshold and measured the mode excitations. This procedure gave us the FSR to within 10 kHz. Next, we placed the cavity just below the lasing threshold and performed spectral measurements following single-site injection, and maximized the transport observed over the modes as we varied the modulation frequency. To measure the FSR of our cavity down to 10 Hz, we modulated the EOM with multiple tones, which increased the sensitivity due to interferences between different paths taken over multiple roundtrips of the cavity. If the modulation is slightly detuned, the transport exhibits effects related to Bloch oscillations, which are much easier to detect than direct resonance. The Supplementary Information provides more details, including measurements of Bloch oscillations (Supplementary Fig. 5). Suppressing these oscillations allowed us to find the FSR to five decimal places, down to 10 Hz.

Set-up modelling

We consider the complex-valued electric field A(x,t) inside the ring cavity such that A(x,t) = A(x+L,t) where L is the roundtrip length of the cavity. In the absence of dispersion, we can expand this electric field in terms of resonant modes as $A(x,t) = \sum_m A(x) a_m(t) \mathrm{e}^{\mathrm{i} m \Omega t}$ due to this periodic boundary condition. Here, Ω is the mode spacing, related to the roundtrip length as $\Omega = c/L$. In the frequency domain, the resonant modes a_m are then coupled via a phase modulator to realize a variety of tight-binding graphs. In the time domain, the action of the phase modulator over one roundtrip is simply $a(t+\tau) = \mathrm{e}^{\mathrm{i} \phi(t)} a(t)$, where the cavity modulation $\phi(t)$ is proportional to the RF signal v(t) driving the phase modulator and is periodic over the roundtrip time τ . In the basis of the frequency modes, this action is described by

$$U = e^{iJ\tau} = F^{\dagger} e^{iV} F \tag{3}$$

where V is a diagonal operator encoding the modulation $\phi(t)$ along the diagonal, and F is the discrete Fourier transform $F_{jk} = (e^{-i2\pi t/N})^{jk}$, where N is the number of modes. The equation above sets constraints on the time evolution operator U, namely that it is a unitary Toeplitz operator, that is, a unitary matrix with constant diagonals.

For small values of the matrix J, the full coupled mode equations are

$$\dot{a_m}(t) = \left(im\Omega - \frac{g}{1 + \sum_n |a_n|^2 / P_{\text{sat}}} - \ell\right) a_m(t) - i \sum_n J_{n-m} a_n(t) + a_{\text{in}}(t) e^{i\Delta t}$$
(4)

where g is the small-signal gain, ℓ is the roundtrip loss, $a_{\rm in}$ is a complex frequency-dependent amplitude encoding the input state at frequency $\omega_{\rm in}$, $P_{\rm sat}$ is the nonlinear saturating gain, and Δ is the detuning between the seed and the cavity frequency. The term J_k describes the coupling terms from the phase modulator, given by $J_k = (2\pi)^{-1} \int_0^{1/\Omega} {\rm d}t e^{i\phi(t)} e^{ik\Omega t}$. To model the effect of dispersion we would include a term proportional to m^2 in the first term, but we have not done so because in our experiments the dispersion was sufficiently small that it could be neglected.

This equation is simplified by moving to the rotating frame of each mode $a_m(t) \rightarrow a_m(t) e^{im\Omega t}$ and operating well below the saturation power. In this form, the equations reduce to

$$\vec{a_m}(t) = -\gamma a_m(t) - i \sum_n J_{n-m} a_n(t) + a_{\rm in}(t) e^{i\Delta t}$$
 (5)

where $\gamma = \ell - g$ is the gain–loss balance, and Δ is the detuning from the cavity modes. Collecting the mode amplitudes in a column vector $|a(t)\rangle = (a_0(t), a_1(t), ...)^\mathsf{T}$ with the basis $\{|m\rangle\}$ indexing the cavity modes, we obtain

$$i\langle m|\left(\frac{\partial}{\partial t} - i\gamma + f\right)|a(t)\rangle = \langle m|a_{\rm in}\rangle e^{i\Delta t} \tag{6}$$

In this basis, $|a_{\rm in}\rangle$ is a column vector encoding the injection. For a continuous wave injection, $|a_{\rm in}\rangle=(0,\,0,\,...,\,0,\,a_{\rm in},\,0,\,...)^{\rm T}$. Neglecting the loss in the system, the equation above describes the Schrödinger equation derived from the Hamiltonian in equation (1), with H=J. The implicit assumption is that because the Hamiltonian is sufficiently linear, the many-body states are described with just a single-excitation picture, that is, with first quantization.

Equation (6) has a simple steady-state solution in the continuous limit for a single-site injection, that is, $|a_{\rm in}\rangle = (0, 0, ..., 0, 1, 0, ..., 0, 0)^{\rm T}$. Substituting the basis vectors $\{\langle m | \}$ indexing the mode numbers with

a continuous parameter x, we can integrate equation (6) with Fourier transforms to obtain

$$a(x, t \to \infty) = i\sqrt{P_{\text{in}}} \int \frac{dk \, e^{ikx}}{\phi_k - i\gamma}$$
 (7)

where ϕ_k is the spectrum of J. For example, for a 1D nearest-neighbour coupling with strength J_0 , where $\phi_k = k^2$, equation (7) has the steady-state solution

$$a(x) = \pi \sqrt{P_{\text{in}}} \frac{e^{-\sqrt{2\gamma/J_0}|x|}}{2\gamma/J_0}$$
 (8)

where x is the continuous variable indexing the mode number. Clearly, by taking $y \rightarrow 0$, that is, operating at threshold, the number of occupied modes reaches infinity. Of course, the solution in equation (8) neglects the effects of dispersion and, more importantly, gain saturation. From simulations, we found that dispersion would begin limiting our lattice sizes around a bandwidth of -100 GHz, but that the gain saturation limits the size much earlier, effectively increasing the loss as discussed above.

Figure 4 shows the correlations of a simple 1D lattice with either nearest-neighbour hoppings or next-nearest-neighbour hoppings. These matrices are constructed from the measured spectral response of the lattice at a given injection site:

$$G_{ij} = \langle n(i)^* n(j) \rangle - \langle n(i)^* \rangle \langle n(j) \rangle$$
(9)

where n(j) denotes the population at site j, and $n(i)^*$ denotes the population at site i given the injection was made at site i, and the $\langle ... \rangle$ brackets denote the average over injection sites. We denote these quantities as the non-equilibrium correlation matrices, and find these measurements capture correlations of systems also found in other literature.

Real-space-occupation and bandstructure measurements

To map the power spectrum to the occupation at a particular lattice site, the peak of the power around a neighbourhood of the expected frequency of the cavity mode was picked. To generate lattice plots in 2D and higher, we employed this prescription to retrieve the peaks from a 1D chain, then reshaped the data appropriately depending on the type of lattice the coupling signal realizes. For example, if we measure the response in a 2D square lattice, where we modulate the cavity at Ω and $L\Omega$, we pick $N = L \times L$ peaks of the spectrum, and wrap them in an $L \times L$ matrix.

To instantiate a triangular lattice, we modulate the intracavity EOM at three frequencies $\{\Omega, L\Omega, (L+1)\Omega\}$, a 2D square lattice with extra diagonal connections. By choosing the relative values of the coupling, the connectivity of this graph can be made exact with the connectivity of a triangular lattice. However, the six-fold symmetry of this lattice is not captured when presented in regular euclidean space. Thus, beginning with every even row of our lattice, we shift the indices over by one, as shown in Supplementary Fig. 8, resulting in the expectant traversals. Doing so preserves the local connectivity of the triangular lattice without physically altering the connectivity.

To measure the bandstructure, the output of the cavity is amplified and filtered with a 0.1–1-GHz bandpass filter in the RF domain. The amplifier increases the signal-to-noise ratio needed for the single-shot readout for the bandstructure measurements. Single-shot readout is needed due to the phase walk-off between the injection and the cavity. For details of the bandstructure measurements, we refer to ref. 22, but we briefly summarize the procedure here and outline our extensions for measurements of bandstructures in 2D and higher.

The modulation signal to realize a 30×30 2D square lattice is $v_{\rm 2D}(t) = V_{\rm 1} \cos(\Omega t) + V_{\rm 2} \cos(30\Omega t)$, as shown in Supplementary Fig. 9a. The output of the cavity is measured with an oscilloscope to produce the raw measurement of a 1D time series (Supplementary Fig. 9b). This

time series is then divided into chunks set by the cavity roundtrip time $\tau=1/\Omega$. Here, we scanned over one mode in 1 ms. These two timescales were observed to be well separated enough to allow the laser to find equilibrium with the continuously changing scanning frequency. The widths of the bandstructures are proportional to $\Omega V/V_{\pi}$, where V is the modulation amplitude and V_{π} is the pi-voltage of the phase modulator. For all bandstructure measurements we drove the EOM very close to the pi-voltage to obtain wide bandstructures.

A real 2D square lattice has a bandstructure of $E(k) = -2J\cos(k_x a) - 2J\cos(k_y a)$, but the above produces only a single dimension. To construct the full 2D bandstructure from this signal, we again separate the time-domain response signal into two timescales. The timescale measuring the cavity response over just a single roundtrip is decomposed into L chunks, so that each chunk is of length $t_{\rm fast} = 1/L\Omega$, where L is the secondary long-range coupling used to instantiate a 2D square lattice. The secondary timescale is synthetically formed by looking at points separated by $1/L\Omega$. In other words, if we reconstruct the full 2D bandstructure by appending chunks of length $t_{\rm fast}$, $t_{\rm slow}$ is the orthogonal direction pointing along the different chunks. These two timescales, $t_{\rm fast}$ and $t_{\rm slow}$, map to the two independent momenta k_x and k_y , when the timescales are well separated enough, as is the case for $L \gg 1$. See Methods and Supplementary Figs. 9, 10 and 12 for full details of this reconstruction

To take paths through the high symmetry points of the Brillouin zone, high-resolution experimental data are needed. For the bandstructure measurements, the cavity was modulated at a slightly detuned frequency (-10–20 Hz) to match with a multiple of the sampling rate of the oscilloscope. This also prevented a walk-off in the reconstructions when the scope sampling rate was detuned from the cavity-mode spacing, leading to a linear shift in the bandstructure along $t_{\rm slow}$ when digitized.

Input-state preparation

To prepare arbitrary input states, a high modulation bandwidth and high preparation fidelity, with no spurious images or modes, are required. To this end, we implemented an image rejection IQ mixer in the optical domain by combining a 12-GHz phase modulator with a fibre Bragg grating as a filter (Supplementary Fig. 12). The Bragg grating is a 4-GHz bandpass filter centred 12 GHz away from the injection, enabling programmability input states in -4,000 lattice sites, while rejecting the spurious sidebands in addition to the carrier frequency. The baseband signal around a 12-GHz tone was encoded in a voltage signal from an AWG as I and Q pairs and upconverted with an electronic IQ mixer. The resultant upconverted signal was then sent to drive the external EOM, enabling both phase and amplitude programmability of the input state at every lattice position.

To account for spectral inhomogeneities in the input chain, we calibrated the modulation by measuring the light before entering the cavity. If the modulation has some inhomogeneity, such that a voltage signal $V(t) = \sum_n V_n \sin(n\Omega t)$ is modified to $V(t) = \sum_n (V_n \eta_n) \sin(n\Omega t)$, the output power in each mode is scaled by η_n^2 . To compensate, we injected light that had been uniformly modulated at all integer multiples of the FSR within the spectral region of interest, that is, a top hat distribution defined on lattice sites. This region of interest contains roughly up to 2,000 modes for the input states presented in Fig. 3b. The square root of the response of this measurement gives us $\neg \eta_n$, which we used to apply an envelope function to the modulation signal. If successful, a top hat modulation multiplied with this envelope function will produce a clean flat spectrum. Otherwise, this process can be iterated for higher order.

The phase modulator preparing input states and the phase modulator programming the cavity interactions are synced to the same clock; however, the voltage signal driving the input-state modulator is upconverted before hitting the EOM. This imparts a phase difference between the input state and the cavity due to the different cable lengths. The phase difference between the injected light and the cavity defines the average momentum of the excitation. To account for this

delay, we prepared a state with net-zero momentum (in the frame of the outgoing signal) into a tight-binding lattice, and tuned the phase of the cavity signal until we observed no transport.

Data availability

All data generated used in this work are available at https://doi.org/10.5281/zenodo.6959554.

Code availability

All code used in this work are available at https://doi.org/10.5281/zenodo.6959554.

Acknowledgements

P.L.M. acknowledges financial support from a David and Lucile Packard Foundation Fellowship, and also membership of the CIFAR Quantum Information Science Program as an Azrieli Global Scholar. We thank NTT Research for their financial and technical support. Portions of this work were supported by the National Science Foundation (award CCF-1918549). We acknowledge helpful discussions with D. Hathcock, E. Mueller, S. Prabhu, E. Rosenberg and members of the NTT PHI Lab/NSF Expeditions research collaboration. We also thank A. Dutt for helpful discussions and for feedback on a draft of the manuscript. We thank M. Buttolph for assistance with fibre splicing and V. Tjong for contributing to the instrumentation-control code.

Author contributions

A.S., L.G.W. and P.L.M. developed the concept. A.S. and L.G.W. built the experimental set-up, with early contributions from H.K.D. A.S. performed the experiments, the data analysis and the numerical simulations (theory). P.F.W. performed experimental data collection. A.S., L.G.W. and P.L.M. wrote the manuscript. L.G.W. and P.L.M. supervised the project.

Competing interests

The authors declare no competing interests.

Additional information

Supplementary information The online version contains supplementary material available at https://doi.org/10.1038/s41567-023-02075-7.

Correspondence and requests for materials should be addressed to Alen Senanian or Peter L. McMahon.

Peer review information *Nature Physics* thanks the anonymous reviewers for their contribution to the peer review of this work

Reprints and permissions information is available at www.nature.com/reprints.